

ABAQUS UELMAT subroutine for implementing phase field fracture

Emilio Martínez-Pañeda^{a,*}

^a*Department of Civil and Environmental Engineering, Imperial College London, London SW7 2AZ, UK*

Abstract

Documentation that accompanies the UELMAT subroutine provided to implement the phase field fracture method in ABAQUS in combination with any material model available in ABAQUS. The code can be downloaded from www.empaneda.com/codes. If using these codes for research or industrial purposes, please cite the following articles:

M. Simoes, C. Braithwaite, A. Makaya, E. Martínez-Pañeda. Modelling fatigue crack growth in Shape Memory Alloys. *Fatigue & Fracture of Engineering Materials & Structure* 45: 1243-1257 (2022)

Z. Khalil, A.Y. Elghazouli, E. Martínez-Pañeda. A generalised phase field model for fatigue crack growth in elastic-plastic solids with an efficient monolithic solver. *Computer Methods in Applied Mechanics and Engineering* 388, 114286 (2022)

Contents

1	Introduction and list of files	1
2	Phase field fracture: theory and implementation	3
2.1	Weak and strong formulations	3
2.2	Finite element implementation	4
3	Usage instructions	4
4	Representative examples	7
4.1	Shape Memory Alloys: crack growth in a single edge notched sample	7
4.2	Combined isotropic and kinematic hardening: failure of an asymmetrically notched plate	8

1. Introduction and list of files

The phase field fracture method has attained notable popularity. By smearing sharp interfaces such as cracks over a finite distance and using an auxiliary phase field variable ϕ to track their evolution, complex phenomena can be predicted such as crack branching, nucleation of secondary cracks and the coalescence of multiple defects. Although first proposed as a regularisation of Griffith's

*Corresponding author.

Email address: e.martinez-paneda@imperial.ac.uk (Emilio Martínez-Pañeda)

energy balance [1], its success has quickly been extended to numerous materials and applications; examples include fibre-reinforced composites [2, 3], hydrogen embrittlement [4–6], batteries [7, 8], rock-like materials [9, 10], functionally graded materials [11–13], corrosion [14], fatigue damage [15, 16] and shape memory alloys [17] - see [18, 19] for an overview. Thus, there is a need to develop suitable computational schemes that can easily couple the phase field evolution equation with a wide range of material models. This is the goal of the code that accompanies this documentation.

The `UEL` subroutine is a user subroutine to define an element with access to ABAQUS material models. The `UEL`, similar to user element (`UEL`) subroutines, requires defining the element residual and stiffness matrices. However, the `UEL` differs from the `UEL` in that it enables access to the ABAQUS's material library (`materiallibmech`). This can be exploited to readily obtain the (undamaged) stress tensor $\boldsymbol{\sigma}_0$ and material Jacobian \mathbf{C} for (in-built) material models of arbitrary complexity, without the need to implement advanced constitutive laws and integration schemes. Specifically, we demonstrate the potential of this approach by simulating cracking in non-linear kinematic/isotropic hardening solids [20] and in Shape Memory Alloys (SMAs) [21]. Two aspects should be emphasised:

- The use of `UEL` subroutines comes with a very high RAM consumption. This is the result of a bug (memory leak) that ABAQUS fixed in the last release of the 2021 version (R2021xFP.CFA.2050 HotFix5). I.e., for older ABAQUS versions, running large models will require access to computers with high RAM capacity.
- If the material model is not complex or is available (e.g., a `UMAT` subroutine), then other approaches are typically more competitive. For example, the implementation of phase field in ABAQUS is greatly simplified when adopting `UMAT`- or `HETVAL`-based approaches [22, 23]. Alternatively, the use of a `UEL` subroutine provides more flexibility and enables the use of efficient quasi-Newton monolithic solution schemes [24] (which can also be used with `UEL`).

The remaining part of the documentation includes: (i) a brief introduction to phase field and its numerical implementation (Section 2), (ii) the usage instructions (Section 3), and (iii) representative numerical examples (Section 4). To simplify the understanding of the code and the documentation, everything is formulated for the case of the so-called `AT2` or conventional phase field fracture model and without considering any strain energy decomposition; however, more general codes involving other phase field models (`AT1` [25], `PF-CZM` [26], etc.) and strain energy splits (volumetric-deviatoric [27], spectral [28], etc.) can be provided upon request (e.martinezpaneda@imperial.ac.uk). The following files are provided:

`UEL` - simple `UEL` subroutine with the standard (`AT2`) phase field model.

`Job-1.inp` - simple input file to simulate mode I crack growth in a single edge notched tension SMA specimen (see Section 4.1).

`Job-2.inp` - simple input file to simulate the failure of an asymmetric double notched bar sample exhibiting non-linear kinematic and isotropic hardening (see Section 4.2).

For simplicity, the subroutine is coded in such a way that can be used for both Shape Memory Alloys and metals exhibiting non-linear kinematic and isotropic hardening, with the driving force

for fracture being the total strain energy density (including inelastic contributions). Other versions can be provided upon request.

2. Phase field fracture: theory and implementation

2.1. Weak and strong formulations

The purpose of the phase field approximation is to regularise the fracture energy, with the phase field ϕ acting as a scalar damage variable (from 0 at intact material points to 1 inside the crack) and the size of the regularized crack surface being governed by the choice of a phase field model-inherent length scale ℓ . The total potential energy of a cracked solid, composed of the bulk $\Psi^b(\mathbf{u}, \phi)$ and fracture $\Psi^s(\phi)$ energies, is then defined as

$$\Psi = \Psi^b(\mathbf{u}, \phi) + \Psi^s(\phi) = \int_{\Omega} \left[(1 - \phi)^2 \psi(\mathbf{u}) + G_c \left(\frac{\phi^2}{2\ell} + \frac{\ell}{2} |\nabla \phi|^2 \right) \right] dV \quad (1)$$

where \mathbf{u} is the displacement field, G_c is the material toughness and ψ is the strain energy density. While phase field was initially postulated as an approximation to Griffith fracture in ideally brittle solids, the formulation is general; the driving force for fracture can be enriched to include any arbitrary variable and the fracture resistance G_c can be chosen much larger than the surface energy (e.g., to account for the effects of plasticity, as first postulated by Orowan [29]). Thus, (1) holds in the presence of any inelastic quantity, such that the stress tensor $\boldsymbol{\sigma} = \partial_{\boldsymbol{\varepsilon}} \psi$ equals

$$\boldsymbol{\sigma} = \mathbf{C}\boldsymbol{\varepsilon} = \mathbf{C}^e \boldsymbol{\varepsilon}^e = \mathbf{C}^e \boldsymbol{\varepsilon}^e = \mathbf{C}^e (\boldsymbol{\varepsilon} - \boldsymbol{\varepsilon}^p) \quad (2)$$

where \mathbf{C}^e is the elastic stiffness tensor, and $\boldsymbol{\varepsilon}^e$ and $\boldsymbol{\varepsilon}^p$ are the elastic and inelastic strain tensors. The total strain tensor being given by $\boldsymbol{\varepsilon} = \text{sym} \nabla \mathbf{u}$. Inelastic contributions can drive fracture; e.g., assuming that ψ is the driving force for fracture, then

$$\psi = \int_0^t (\boldsymbol{\sigma} : \boldsymbol{\varepsilon}) dt = \psi^e + \psi^p = \frac{1}{2} \boldsymbol{\varepsilon} : \mathbf{C}^e : \boldsymbol{\varepsilon} + \int_0^t (\boldsymbol{\sigma} : \boldsymbol{\varepsilon}^p) dt \quad (3)$$

where ψ^p is the inelastic strain energy density. It can be readily seen that the history-dependency comes into play via the inelastic contribution. Now, taking the first variation of the total potential energy of the solid (Eq. (1)) with respect to $\boldsymbol{\varepsilon}$ and ϕ renders the weak form of the deformation-phase field fracture problem. Thus, in the absence of body forces and external tractions,

$$\int_{\Omega} \left\{ (1 - \phi)^2 \boldsymbol{\sigma} : \delta \boldsymbol{\varepsilon} - 2(1 - \phi) \delta \phi \psi + G_c \left(\frac{\phi}{\ell} \delta \phi + \ell \nabla \phi \cdot \nabla \delta \phi \right) \right\} dV = 0 \quad (4)$$

Upon making use of Gauss' divergence theorem, the following coupled field equations are obtained for any arbitrary value of the kinematic variables $\delta \mathbf{u}$ and $\delta \phi$,

$$\begin{aligned} (1 - \phi)^2 \nabla \cdot \boldsymbol{\sigma} &= \mathbf{0} \quad \text{in } \Omega \\ G_c \left(\frac{\phi}{\ell} - \ell \nabla^2 \phi \right) - 2(1 - \phi) \psi &= 0 \quad \text{in } \Omega \end{aligned} \quad (5)$$

2.2. Finite element implementation

Let us now adopt the following finite element discretisation for the primary kinematic variables and their derivatives. Using Voigt notation, the nodal values of the displacements, strains, phase field and phase field gradients are interpolated as follows,

$$\mathbf{u} = \sum_{i=1}^m \mathbf{N}_i \mathbf{u}_i, \quad \phi = \sum_{i=1}^m N_i \phi_i, \quad \boldsymbol{\varepsilon} = \sum_{i=1}^m \mathbf{B}_i^u \mathbf{u}_i, \quad \nabla \phi = \sum_{i=1}^m \mathbf{B}_i \phi_i \quad (6)$$

where m is the number of nodes, \mathbf{B}_i are vectors with the spatial derivatives of the shape functions, \mathbf{B}_i^u denotes the standard strain-displacement matrices and \mathbf{N}_i are the interpolation matrices - diagonal matrices with the nodal shape functions N_i as components. To ensure damage irreversibility, a history field \mathcal{H} can be defined [28]. Here, let's assume for simplicity that this irreversibility constraint is applied to the total strain energy density, such that for a time t :

$$\mathcal{H} = \max_{t \in [0, t]} \psi(t). \quad (7)$$

Making use of the finite element discretization outlined above and considering that Eq. (4) must hold for arbitrary values of $\delta \mathbf{u}$ and $\delta \phi$, one reaches the following residuals:

$$\mathbf{r}_i^u = \int_{\Omega} \left\{ [(1 - \phi)^2 + \kappa] (\mathbf{B}_i^u)^T \boldsymbol{\sigma} \right\} dV \quad (8)$$

$$r_i^\phi = \int_{\Omega} \left[-2(1 - \phi) N_i \mathcal{H} + G_c \left(\frac{\phi}{\ell} N_i + \ell \mathbf{B}_i^T \nabla \phi \right) \right] dV \quad (9)$$

with κ being a sufficiently small numerical parameter introduced to keep the system of equations well-conditioned. Finally, the components of the consistent stiffness matrices can be obtained by differentiating the residuals with respect to the incremental nodal variables:

$$\mathbf{K}_{ij}^u = \frac{\partial \mathbf{r}_i^u}{\partial \mathbf{u}_j} = \int_{\Omega} [(1 - \phi)^2 + \kappa] (\mathbf{B}_i^u)^T \mathbf{C} \mathbf{B}_j^u dV \quad (10)$$

$$\mathbf{K}_{ij}^\phi = \frac{\partial r_i^\phi}{\partial \phi_j} = \int_{\Omega} \left[\left(2\mathcal{H} + \frac{G_c}{\ell} \right) N_i N_j + G_c \ell \mathbf{B}_i^T \mathbf{B}_j \right] dV \quad (11)$$

where \mathbf{C} is the elastic-plastic consistent material Jacobian.

3. Usage instructions

The phase field model is implemented using a `UEL` subroutine. For simplicity, the files provided are limited to 2D plane strain conditions but the extension to 3D is straightforward. We consider isoparametric 2D quadrilateral elements (linear and quadratic) with 3 degrees of freedom per node, i.e. u_x , u_y and ϕ , and four integration points. A number of history-dependent quantities are stored as solution-dependent state variables `SVARS`, these are given in Table 1. The stress variables refer to the undamaged stress tensor $\boldsymbol{\sigma}_0$.

As with user element (`UEL`) subroutines, `UEL` subroutines have the drawback that integration point variables cannot be visualized in `ABAQUS/Viewer`. This limitation is intrinsic to the fact that the only information that `ABAQUS` requests from the subroutine are the stiffness matrix and the right-hand side nodal force vector - the magnitude of the stresses and the strains, as

Variable	SVARS numbering
Axial stresses - σ_{11} , σ_{22} , σ_{33}	SVARS(1), SVARS(2), SVARS(3)
Shear stress - σ_{12}	SVARS(4)
Axial strains - ε_{11} , ε_{22} , ε_{33}	SVARS(5), SVARS(6), SVARS(7)
Shear strain - ε_{12}	SVARS(8)
Crack phase field - ϕ	SVARS(9)
History variable field - H	SVARS(10)
Total strain energy density - ψ	SVARS(11)

Table 1: List of solution dependent state variables for the UEL.

well as the choice of shape functions, is information that is not available as output. To overcome this limitation, we here make use of an auxiliary dummy mesh consisting of standard ABAQUS elements that resemble the user defined element in terms of number of nodes and integration points (i.e., CPE4 or CPE8R). The material response at each integration point in the auxiliary mesh is defined using a user material subroutine (**UMAT**), which enables the user to define the constitutive matrix and the stresses from the strain values. In this auxiliary mesh, the stress components and the constitutive matrix are made equal to zero (i.e., they have no influence in the solution of the global system). The data from our **UEL** that we want to observe in ABAQUS/Viewer is stored in a Fortran module, which allows transferring to the **UMAT** subroutine. In the **UMAT** the information is passed to the built-in array **STATEV** for each corresponding element and integration point. If SDV variables are requested as Field Output we would be able to visualize the results. Table 2 shows the equivalence between model variables and SDVs.

Variable	SDVs numbering
Axial stresses - σ_{11} , σ_{22} , σ_{33}	SDV1, SDV2, SDV3
Shear stress - σ_{12}	SDV4
Axial strains - ε_{11} , ε_{22} , ε_{33}	SDV5, SDV6, SDV7
Shear strain - ε_{12}	SDV8
Crack phase field - ϕ	SDV9
History variable field - H	SDV10
Total strain energy density - ψ	SDV11

Table 2: List of solution dependent state variables.

The first step is to create the model in ABAQUS/CAE. The procedure is the same as with standard ABAQUS models with the following subtleties:

- Two materials should be defined. The first one (**Material-1**) is defined in the usual manner, taking advantage of the in-built material library of ABAQUS (e.g., SMAs, combined kinematic-isotropic hardening, etc.). The other one (**Material-2**) has to be defined as a user material with 11 solution-dependent variables. (General \rightarrow Depvar: 11 & General \rightarrow User Material - Mechanical Constants: 0).
- SDV, Solution dependent state variables, have to be requested as Field Output (as well as displacement, reaction forces and other relevant quantities). (Field Output Request - State/Field/User/Time: SDV, Solution dependent state variables)

- The (Static, General) Step definition varies depending on the solution scheme. If a staggered approach is used, then one should define the incrementation type as “Fixed” (as opposed to “Automatic”) to use a constant time increment. Automatic time stepping can be used when using a monolithic quasi-Newton approach, which requires selecting ‘Solution technique: quasi-Newton’ in the tab ‘Other’.
- The mesh has to be very refined in the expected crack propagation area. As discussed in our publication, the characteristic element size has to be at least 5 times smaller than ℓ to resolve the fracture process zone [30]. If the crack path is unknown a common strategy is to start with a coarser uniform mesh and refine in subsequent calculations. Use as element type CPE4 or CPE8R.

Once the model has been developed, we create a job and write the input file (Right click on the Job name and click “Write Input”). A few modifications have to be done to the input file to define the user element, the use of a code editor like Notepad++ is recommended. First, we create the dummy visualization mesh. For this purpose we use the Matlab script VirtualMesh.m, which is part of the Abaqus2Matlab package [31]. Running VirtualMesh.m on the same folder as the input file (Job-1.inp) will create a new file (VisualMesh.inp) with the element connectivity of the visualization mesh.

The first step is to replace the element type,

```
*Element, type=CPE4
```

with the user element definition,

```
*User element, nodes=4, type=U1, properties=3, coordinates=2, var=44,
  INTEGRATION=4, TENSOR=PSTRAIN
1,2
1,3
*ELEMENT, TYPE=U1, ELSET=SOLID
```

where we have defined the number of nodes (linear version), the number of properties that will be defined in the input file, the number of coordinates (2D), and the number of **SVARS** (11 per integration point). Also, note that **UEL** subroutines require the definition of the number of integration points (here, 4, assuming full integration) and the relevant stress state assumed (plane strain in this case). For a 3D element one would write **TENSOR=THREED**. We have defined the ordering of the DOFs in a way such that the variable **U** contains the components: $u_x^1, u_y^1, u_x^2, u_y^2, u_x^3, u_y^3, u_x^4, u_y^4, \phi^1, \phi^2, \phi^3$ and ϕ^4 . Accordingly, if one wishes to prescribe a cracked region through the phase field parameter, the boundary condition $\phi = 1$ should be enforced on the DOF 3.

After the element connectivity list one inserts,

```
*UEL PROPERTY, ELSET=SOLID, MATERIAL=Material-1
0.024, 2.7, 0
*Element, type=CPE4, elset=Visualization
```

and immediately afterwards the visualization connectivity list (i.e., the content of the file VisualMesh.inp created by the Matlab script). Here, we have defined the user element properties following Table 3. Throughout our model we employ SI (mm) units.

UEL PROPERTY	Description
PROPS(1)	ℓ - Phase field length parameter [mm]
PROPS(2)	G_c - Critical energy release rate [MPa mm] (or kJ/m ²)
PROPS(3)	Solution flag variable (0 - monolithic, 1 - staggered)

Table 3: List of user element properties.

And finally, note that, since we have defined our dummy connectivity list within the element set “Visualization”, we need to modify the Section definition,

```
*Solid Section, elset=Set-1, material=Material-1
```

to change the name of the element set,

```
*Solid Section, elset=Visualization, material=Material-2
```

Additionally, one should note that a Fortran module has been defined in the first lines of the subroutine for visualization purposes. One has to be sure that the first dimension of the variable `UserVar` is larger than the total number of elements.

We emphasise that the steps described are identical for the case studies considered here: (i) a solid described by a combined non-linear kinematic/isotropic hardening law, and (ii) a shape memory alloy. The same user subroutine is used for both and the only difference lies in the definition of `Material-1`. For simplicity, in both cases we assume that the driving force for fracture corresponds to the total strain energy density - this is different from the assumptions made our papers [20, 21] (the specific codes employed can be provided upon request).

4. Representative examples

4.1. Shape Memory Alloys: crack growth in a single edge notched sample

A simple benchmark is addressed to showcase the use of the subroutine for Shape Memory Alloys (SMAs) - the reader is referred to Ref. [21] for advanced examples. Specifically, we choose to model a paradigmatic benchmark in the phase field fracture community - a square plate with a horizontal crack. The geometry and boundary conditions are shown in Fig. 1a. The material properties, listed in Table 4, correspond to those of the equiatomic nitinol SMA tested by Strnadel *et al.* [32], as calibrated in our paper (see Refs. [17, 21]). As in the experiments, the simulations are conducted at a temperature of 47 C (320 K), and this is specified in the input file through the application of initial conditions of the type temperature to the entire model. In this representative example, the material toughness is chosen to be $G_c = 2.7$ kJ/m² and the phase field length scale equals $\ell = 0.024$ mm. The load is applied by prescribing a remote vertical displacement of 0.1 mm. A total of 8,532 elements are used to discretise the specimen, with the mesh being refined along the expected crack path. The monolithic quasi-Newton solver is used and the solution is attained requiring only 20 increments. The crack path is shown on the deformed shape of the sample (scale of unity) in Fig. 1b. The force versus displacement response predicted is shown in Fig. 1c. Due the phase transformation of SMAs and the associated toughening, the response deviates from that typically exhibited by linear elastic materials in this boundary value problem.

Table 4: Material parameters used, following the calibration with the uniaxial stress-strain measurements by Str-nadel *et al.* [32] on an equiatomic nitinol SMA [17, 21].

Parameter	Magnitude
Austenite’s Young’s modulus, E_A (MPa)	41000
Martensite’s Young’s modulus, E_M (MPa)	22000
Austenite’s Poisson’s ratio, ν_A	0.33
Martensite’s Poisson’s ratio, ν_M	0.33
Transformation strain, ε_L	0.0335
Start of transformation stress (Loading), σ_{tL}^s (MPa)	456.5
End of transformation stress (Loading), σ_{tL}^f (MPa)	563.8
Start of transformation stress (Unloading), σ_{tU}^s (MPa)	363
End of transformation stress (Unloading), σ_{tU}^f (MPa)	209
Reference temperature, T_{ref} (K)	320
σ vs T slope (loading), $C_M _{\sigma=300\text{MPa}}$ (MPa/K)	5.5
σ vs T slope (unloading), $C_A _{\sigma=300\text{MPa}}$ (MPa/K)	5.5

4.2. Combined isotropic and kinematic hardening: failure of an asymmetrically notched plate

The use of a UELMAT subroutine to simulate the failure of a metal exhibiting combined non-linear kinematic/isotropic hardening is showcased by simulating crack nucleation and growth in an asymmetrically notched plane strain plate (see Fig. 2a). The double-notched plate is clamped at the bottom end ($u_x = u_y = 0$) and subjected to a vertical displacement u^∞ at the top edge. Two circular notches of radii 2.5 mm have been geometrically introduced. The plate is assumed to be made of a metal characterised by a combined non-linear kinematic/isotropic hardening response. Specifically, the material properties resemble those used in Ref. [20], obtained by calibrating against the experiments by Nip *et al.* on hot-rolled carbon steels [33]. The combined non-linear isotropic/kinematic hardening model in-built in ABAQUS is used to attain a good fit with the experimental data. The magnitudes of the isotropic (Q_∞ , b) and kinematic hardening parameters (C , γ) that provide the best agreement with the experiments are listed in Table 5, together with the initial yield stress σ_0 and the elastic properties (Young’s modulus E and Poisson’s ratio ν). Only one backstress is needed. The fracture behaviour is characterised by a phase field length scale equal to $\ell = 0.2$ mm, $G_c = 22.5$. The monolithic quasi-Newton scheme is used to solve the system of equations, and the model is discretised with a total of 7,874 quadrilateral plane strain linear elements.

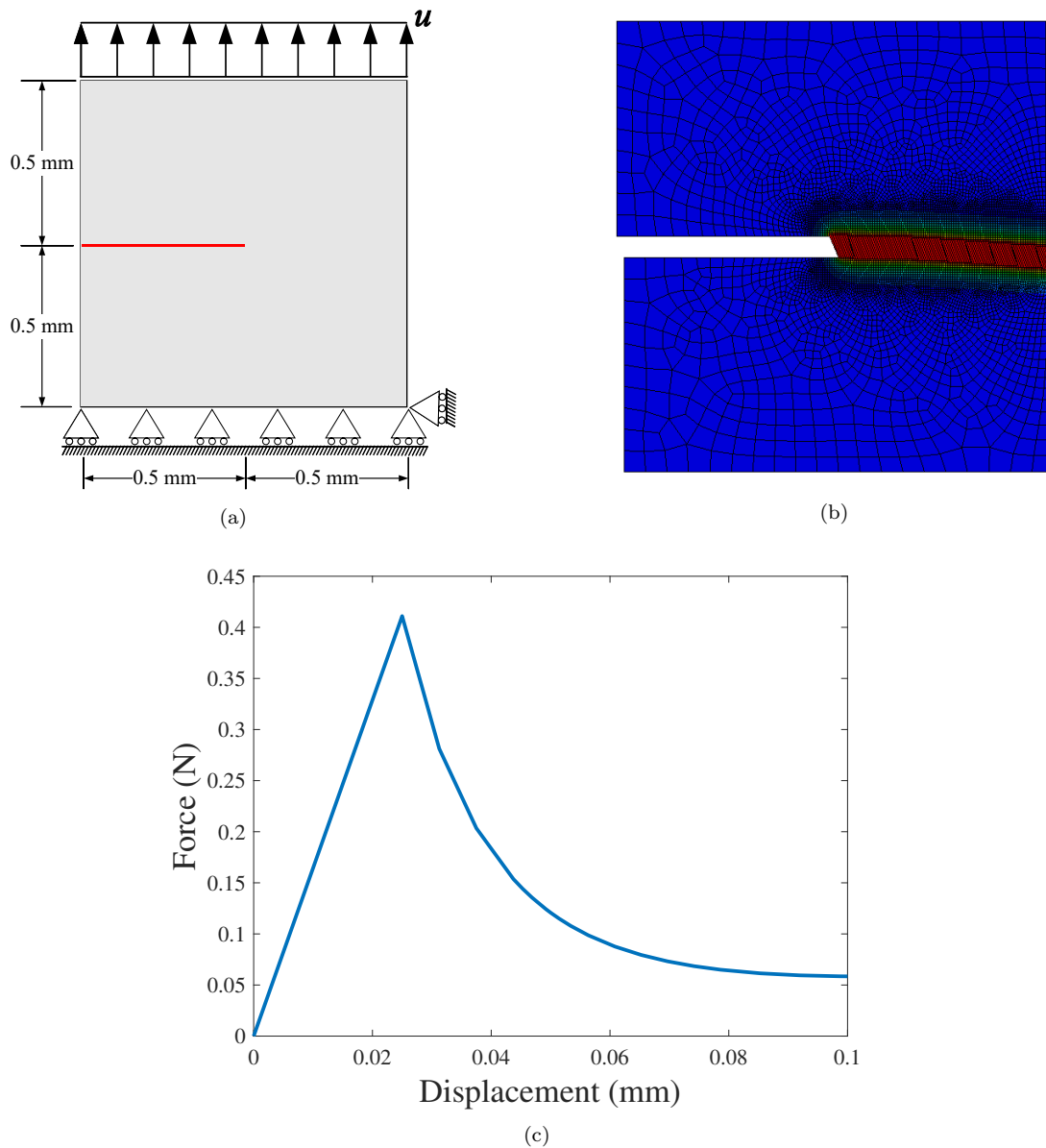


Figure 1: SMA notched square plate under tension: (a) geometry and boundary conditions, (b) contour of the phase field ϕ after rupture (deformed shape), (c) force versus displacement predictions.

Table 5: Material properties used, following calibration with the experiments by Nip *et al.* [33] on a hot-rolled carbon steel exhibiting combined non-linear isotropic/kinematic hardening behaviour [20].

E	ν	σ_0	Q_∞	b	C	γ
[MPa]	[-]	[MPa]	[MPa]	[-]	[MPa]	[-]
215,960	0.3	465	55	2.38	23,554	139

The results obtained are shown in Fig. 2. Specifically, Fig. 2b shows the final cracking pattern on the underformed configuration. Cracks nucleate at the notch tips and suddenly coalesce. The force versus displacement curve obtained is shown in Fig. 2c. Qualitatively, the result is similar to that observed for other materials (e.g., linear elastic solids, SMAs), but some quantitative differences can be observed, associated with the constitutive law adopted and with the adoption

of the total strain energy density as the driving force for fracture (as done here to simplify the understanding of the code).

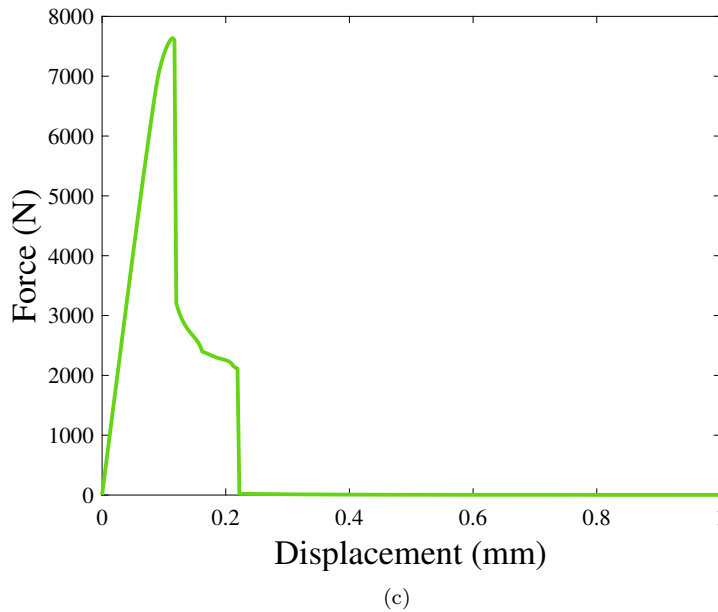
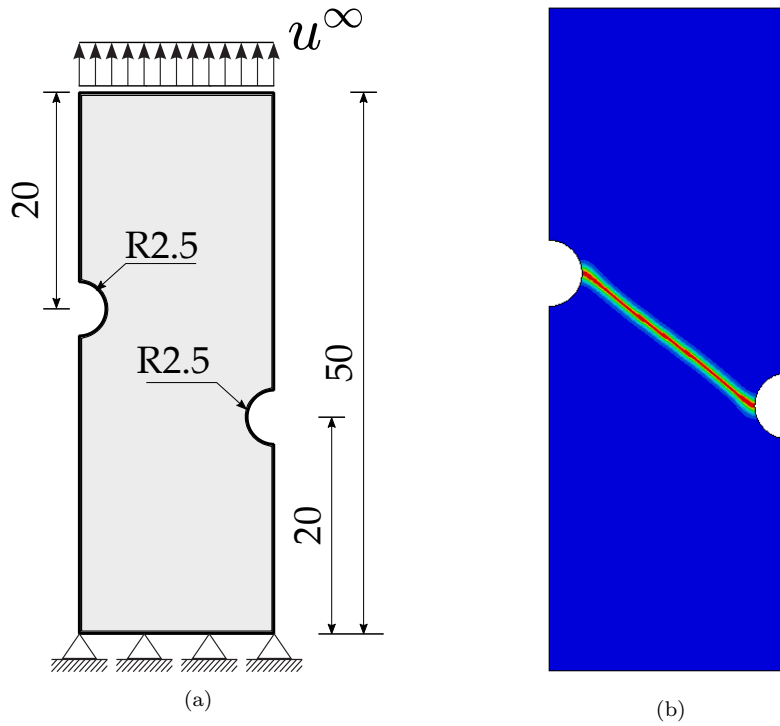


Figure 2: Failure of an asymmetrically notched specimen undergoing combined non-linear kinematic/isotropic hardening: (a) geometry and boundary conditions, (b) contour of the phase field ϕ after rupture (undeformed shape), (c) force versus displacement predictions.

References

- [1] B. Bourdin, G. A. Francfort, J.-J. Marigo, Numerical experiments in revisited brittle fracture, *Journal of the Mechanics and Physics of Solids* 48 (4) (2000) 797–826.

- [2] A. Quintanas-Corominas, J. Reinoso, E. Casoni, A. Turon, J. A. Mayugo, A phase field approach to simulate intralaminar and translaminar fracture in long fiber composite materials, *Composite Structures* 220 (2019) 899–911.
- [3] W. Tan, E. Martínez-Pañeda, Phase field predictions of microscopic fracture and R-curve behaviour of fibre-reinforced composites, *Composites Science and Technology* 202 (2021) 108539.
- [4] P. K. Kristensen, C. F. Niordson, E. Martínez-Pañeda, A phase field model for elastic-gradient-plastic solids undergoing hydrogen embrittlement, *Journal of the Mechanics and Physics of Solids* 143 (2020) 104093.
- [5] P. K. Kristensen, C. F. Niordson, E. Martínez-Pañeda, Applications of phase field fracture in modelling hydrogen assisted failures, *Theoretical and Applied Fracture Mechanics* 110 (2020) 102837.
- [6] M. Isfandbod, E. Martínez-Pañeda, A mechanism-based multi-trap phase field model for hydrogen assisted fracture, *International Journal of Plasticity* 144 (2021) 103044.
- [7] C. Miehe, H. Dal, L.-M. Schanzel, A. Raina, A phase-field model for chemo-mechanical induced fracture in lithium-ion battery electrode particles, *International Journal for Numerical Methods in Engineering* 106 (2016) 683–711.
- [8] M. Klinsmann, D. Rosato, M. Kamlah, R. M. McMeeking, Modeling crack growth during Li insertion in storage particles using a fracture phase field approach, *Journal of the Mechanics and Physics of Solids* 92 (2016) 313–344.
- [9] S. Zhou, X. Zhuang, T. Rabczuk, Phase field modeling of brittle compressive-shear fractures in rock-like materials: A new driving force and a hybrid formulation, *Computer Methods in Applied Mechanics and Engineering* 355 (2019) 729–752.
- [10] L. Schuler, A. G. Ilgen, P. Newell, Chemo-mechanical phase-field modeling of dissolution-assisted fracture, *Computer Methods in Applied Mechanics and Engineering* 362 (2020) 112838.
- [11] Hirshikesh, S. Natarajan, R. K. Annabattula, E. Martínez-Pañeda, Phase field modelling of crack propagation in functionally graded materials, *Composites Part B: Engineering* 169 (2019) 239–248.
- [12] Hirshikesh, E. Martínez-Pañeda, S. Natarajan, Adaptive phase field modelling of crack propagation in orthotropic functionally graded materials, *Defence Technology* 17 (2021) 185–195.
- [13] P. K. A. V. Kumar, A. Dean, J. Reinoso, P. Lenarda, M. Paggi, Phase field modeling of fracture in Functionally Graded Materials: G -convergence and mechanical insight on the effect of grading, *Thin-Walled Structures* 159 (2021) 107234.
- [14] C. Cui, R. Ma, E. Martínez-Pañeda, A phase field formulation for dissolution-driven stress corrosion cracking, *Journal of the Mechanics and Physics of Solids* 147 (2021) 104254.
- [15] P. Carrara, M. Ambati, R. Alessi, L. De Lorenzis, A framework to model the fatigue behavior of brittle materials based on a variational phase-field approach, *Computer Methods in Applied Mechanics and Engineering* 361 (2020) 112731.

- [16] A. Golahmar, P. K. Kristensen, C. F. Niordson, E. Martínez-Pañeda, A phase field model for hydrogen-assisted fatigue, *International Journal of Fatigue* 154 (2022) 106521.
- [17] M. Simoes, E. Martínez-Pañeda, Phase field modelling of fracture and fatigue in Shape Memory Alloys, *Computer Methods in Applied Mechanics and Engineering* 373 (2021) 113504.
- [18] J.-Y. Wu, V. P. Nguyen, C. T. Nguyen, D. Sutula, S. Sinaie, S. Bordas, Phase-field modelling of fracture, *Advances in Applied Mechanics* 53 (2020) 1–183.
- [19] P. K. Kristensen, C. F. Niordson, E. Martínez-Pañeda, An assessment of phase field fracture: crack initiation and growth, *Philosophical Transactions of the Royal Society A: Mathematical, Physical and Engineering Sciences* 379 (2021) 20210021.
- [20] Z. Khalil, A. Y. Elghazouli, E. Martínez-Pañeda, A generalised phase field model for fatigue crack growth in elastic – plastic solids with an efficient monolithic solver, *Computer Methods in Applied Mechanics and Engineering* 388 (2022) 114286.
- [21] M. Simoes, C. Braithwaite, A. Makaya, E. Martínez-Pañeda, Modelling fatigue crack growth in Shape Memory Alloys, *Fatigue & Fracture of Engineering Materials & Structures* 45 (2022) 1243–1257.
- [22] Y. Navidtehrani, C. Betegón, E. Martínez-Pañeda, A unified Abaqus implementation of the phase field fracture method using only a user material subroutine, *Materials* 14 (8) (2021) 1913.
- [23] Y. Navidtehrani, C. Betegón, E. Martínez-Pañeda, A simple and robust Abaqus implementation of the phase field fracture method, *Applications in Engineering Science* 6 (2021) 100050.
- [24] P. K. Kristensen, E. Martínez-Pañeda, Phase field fracture modelling using quasi-Newton methods and a new adaptive step scheme, *Theoretical and Applied Fracture Mechanics* 107 (2020) 102446.
- [25] K. Pham, H. Amor, J. J. Marigo, C. Maurini, Gradient damage models and their use to approximate brittle fracture, *International Journal of Damage Mechanics* 20 (4) (2011) 618–652.
- [26] J.-Y. Wu, A unified phase-field theory for the mechanics of damage and quasi-brittle failure, *Journal of the Mechanics and Physics of Solids* 103 (2017) 72–99.
- [27] H. Amor, J. J. Marigo, C. Maurini, Regularized formulation of the variational brittle fracture with unilateral contact: Numerical experiments, *Journal of the Mechanics and Physics of Solids* 57 (8) (2009) 1209–1229.
- [28] C. Miehe, M. Hofacker, F. Welschinger, A phase field model for rate-independent crack propagation: Robust algorithmic implementation based on operator splits, *Computer Methods in Applied Mechanics and Engineering* 199 (45-48) (2010) 2765–2778.
- [29] E. Orowan, *Fracture and Strength of Solids*, *Reports on Progress in Physics* XII (1948) 185.
- [30] E. Martínez-Pañeda, A. Golahmar, C. F. Niordson, A phase field formulation for hydrogen assisted cracking, *Computer Methods in Applied Mechanics and Engineering* 342 (2018) 742–761.

- [31] G. Papazafeiropoulos, M. Muñoz-Calvente, E. Martínez-Pañeda, Abaqus2Matlab: A suitable tool for finite element post-processing, *Advances in Engineering Software* 105 (2017) 9–16.
- [32] B. Strnadel, S. Ohashi, H. Ohtsuka, S. Miyazaki, T. Ishihara, Effect of mechanical cycling on the pseudoelasticity characteristics of TiNi and TiNiCu alloys, *Materials Science and Engineering A* 203 (1-2) (1995) 187–196.
- [33] K. H. Nip, L. Gardner, C. M. Davies, A. Y. Elghazouli, Extremely low cycle fatigue tests on structural carbon steel and stainless steel, *Journal of Constructional Steel Research* 66 (1) (2010) 96–110.
- [34] K. H. Nip, L. Gardner, A. Y. Elghazouli, Cyclic testing and numerical modelling of carbon steel and stainless steel tubular bracing members, *Engineering Structures* 32 (2) (2010) 424–441.